Unimodal and Well-Defined Nanomicelles Assembled by Topology-Controlled Bicyclic Block Copolymers

Brian J. Ree,[1,*] *Yusuke Satoh*,[2] *Kyeong Sik Jin*,[3] *Takuya Isono*,[1] and *Toshifumi Satoh*[1,*]

[1]Faculty of Engineering, Hokkaido University, Sapporo 060-8628, Japan

[2]Graduate School of Chemical Sciences and Engineering, Hokkaido University, Sapporo 060-8628, Japan

[3]PLS-II Beamline Division, Pohang Accelerator Laboratory, Pohang 37673, Republic of Korea

*Correspondence to: brianree@eng.hokudai.ac.jp (B.J.R.); satoh@eng.hokudai.ac.jp (T.S.)

ABSTRACT: This study provides the first insights into the micellization behavior and micellar morphologies of bicyclic amphiphiles in four different topologies: *bicy*-BCP-A, *bicy*-BCP-B, *bicy*-BCP-C, and *bicy*-BCP-D, consisting of poly(*n*-decyl glycidyl ether) and poly(2-(2-(2-methoxyethoxy)ethoxy)ethyl glycidyl ether) blocks in equivalent molar fractions. Quantitative synchrotron X-ray scattering analysis reveals that all bicyclic amphiphiles self-assemble into unimodal nanomicelles consisting of core, dense corona, and soft corona structural components. The micelles also demonstrate substantial size reductions (56.7–70.7 %) compared to micelles of their linear counterpart (*l*-BCP). The critical micelle concentration, stability, and structural parameters (shape, size, and others) of nanomicelles are differentiated by controlling the bicyclic topology types. *bicy*-BCP-A, -B, and -C form oblate ellipsoidal micelles whereas *bicy*-BCP-D and *l*-BCP assemble into prolate ellipsoidal micelles. The size is found to be in the following order: *bicy*-BCP-D < *bicy*-BCP-C < *bicy*-BCP-B < *bicy*-BCP-A << *l*-BCP. Furthermore, the structural stability is in the following trend: *l*-BCP < *bicy*-BCP-D << *bicy*-BCP-B < *bicy*-BCP-C < *bicy*-BCP-A. These results indicate that the topology-controlled bicyclic block copolymers can be used as a desirable platform for developing high-performance functional core-shell nanoparticles for advanced applications in a variety of fields, including smart drug delivery, biomedical imaging, cosmetics, advanced coating appliances, and molecular electronics.

Keywords: topological bicyclic amphiphiles, synchrotron X-ray scattering, ellipsoidal core-shell micelle, unimodal size distribution, radial density profile

INTRODUCTION

Polymer topology, which describes the shape and spatial features of the polymer main chain, is a crucial factor that affects the physical properties of polymeric materials. Conventional polymers possess a linear topology, while those defined by nonlinear topologies such as cyclic, star, and dendritic features are categorized as topological polymers. Recently, cyclic polymers have garnered attention in research and development of advanced versatile polymers owing to their unique traits (absence of chain ends, compact molecular dimension, high density, high glass transition temperature, and low viscosity).[1-9] The development of cyclic polymer synthesis and various macrocyclization reactions has significantly advanced the efficiency of producing cyclic polymers,[1-5,10-15] and initiated the synthesis of complex variants such as multicyclic homopolymers and copolymers.[4,16-28] Multicyclic polymers impose more constraints on the molecular chain conformation than those imposed by simple monocyclic polymers. However, most of the research on multicyclic polymers has focused on the synthetic aspect. Moreover, owing to the difficulty and complexity of the synthesis, many of the reported multicyclic polymer systems are homopolymers. Therefore, these complex topological polymers require detailed characterization to unveil their fundamental properties, as well as the development and characterization of multicyclic block copolymer systems. The development of block copolymer systems in multicyclic topology is important, as their self-assembly characteristics remain uncharacterized owing to the scarcity of multicyclic block copolymer systems.[29,30] However, the key characteristics of cyclic polymers, such as the absence of chain end groups, can impact the self-assembly and phase-separation behaviors. Further, for multicyclic systems, the molecular joints conjoining the macrocycle subunits affect the self-assembly behavior in different ways. Furthermore, the diverse properties that could emerge from newly developed multicyclic block copolymer systems have great potential for polymer properties and practical applications. Thus, as

the first step in their development, the fundamental characterization of bicyclic block copolymer systems needs to be initiated.

In this study, the micellization of a series of bicyclic block copolymer amphiphiles was subjected to quantitative characterization for the first time. All bicyclic amphiphiles (*bicy*-BCP-A, *bicy*-BCP-B, *bicy*-BCP-C, and *bicy*-BCP-D) as well as their linear analog (*l*-BCP) used as the reference material are composed of hydrophobic poly(*n*-decyl glycidyl ether) (PDGE) and hydrophilic poly(2-(2-(2-methoxyethoxy)ethoxy)ethyl glycidyl ether) (PTEGGE) blocks in equivalent molar fractions (Figure 1). The micellization of individual topological amphiphiles was investigated in an ethanol-water cosolvent system using synchrotron X-ray scattering analysis. Quantitative X-ray scattering analysis offers an extensive range of micellar structural parameters such as overall shape, size distribution, radial density distribution profile, structural subcomponents, blob size, and average chain aggregation number. All amphiphiles were analyzed to determine their micellar morphology based on descriptive structural parameters. Interestingly, the micelles exhibit uniquely diverse structural characteristics, structural integrity, and overall size, depending on the four different variations of the bicyclic topologies.

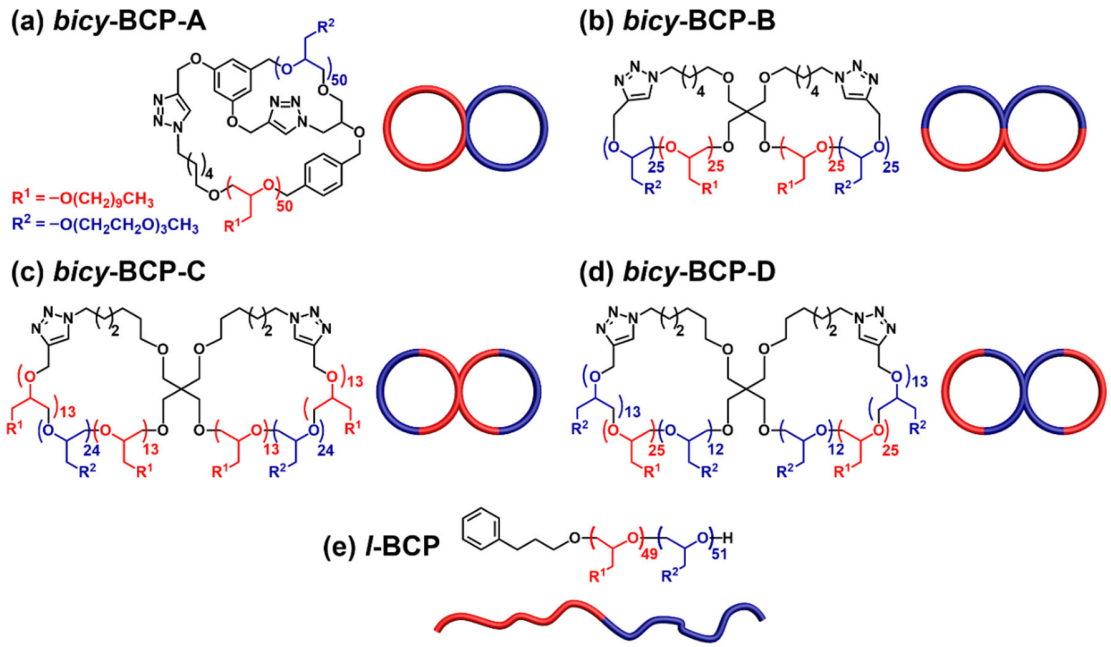

Figure 1. Chemical structures of the topological bicyclic block copolymers and linear block copolymer analogue investigated in this study. The molecular characteristic details of these topological copolymers are given in Table 1.

EXPERIMENTAL SECTION

All topological bicyclic block copolymers and their linear counterparts composed of PDGE and PTEGGE blocks were prepared according to previously reported synthetic schemes.[23,29] The molecular characteristics are summarized in Table 1. The polymers were introduced into various organic solvents and their mixtures to investigate the optimized conditions for micelle formation. They were confirmed to self-assemble successfully as micelles in a mixture of 75 wt% EtOH and 25 wt% H_2O. Further, for the CMC measurement of each polymer, several polymer solutions was prepared over a concentration range of 0.001–0.1 wt%.

For the obtained polymer solutions, X-ray scattering measurements were performed at the 4C beamline[8,32,42-45] of the PLS-II synchrotron facility (operated at a power of 3.0 GeV and 400 mA in top-up mode) of the Pohang Accelerator Laboratory (PAL), Pohang, Republic of Korea. Prior to

measurement, each polymer solution was filtered through a disposable syringe equipped with a polytetrafluoroethylene filter (0.2 μm pore size). The polymer solutions (50 μL) were loaded into quartz capillary tubes (inner diameter, 1.5 mm). All scattering measurements were performed using a synchrotron X-ray radiation source with a wavelength λ of 0.0756 nm at room temperature. The sample-to-detector distances (SDDs) were 4 and 1 m, with the scattering angle being calibrated using precalibrated polystyrene-*b*-polyethylene-*b*-polybutadiene-*b*-polystyrene block copolymer and silver behenate powder (Tokyo Chemical Industry (TCI), Tokyo, Japan) as the standards, respectively. Raw scattering data were collected over 30–60 s of exposure time into a two-dimensional (2D) charge-coupled detector (CCD) (Rayonix 2D Mar, Evanston, IL, USA). Further, 1D scattering profiles were obtained from the circular averaging of the measured 2D scattering data with respect to the beam center, followed by intensity normalization using the intensity of the transmitted X-ray beam monitored through a scintillation counter positioned downstream. The scattering data of the polymer solutions were further corrected for scattering originating from the solvent.

RESULTS AND DISCUSSION

All topological bicyclic and linear block copolymers based on a pair of nonpolar and polar monomers, *n*-decyl glycidyl ether (DGE) and 2-(2-(2-methoxyethoxy)ethoxy)ethyl glycidyl ether (TEGGE), were prepared and characterized as previously reported.[23,29] Proton nuclear magnetic resonance (^{1}H NMR) spectroscopy analysis was used to determine the number-average degrees of polymerization (*DP*) of PGDE and PTEGGE blocks in all block copolymers, which ranged from 48 to 52. Further, the number-average molecular weights ($M_{n,NMR}$) of the block copolymers ranged from 21,800 to 22,300. In addition, the dispersity values ($Đ$) of the individual copolymers were determined to be between 1.03 and 1.06. The complete molecular characteristics are summarized in Table 1. Overall, well-defined bicyclic and linear block copolymers were obtained.

Table 1. Molecular characteristics, degree of polymerization, and volume fractions of bicyclic block copolymers and their linear counterpart[8,23,29]

Topological copolymer	$M_{n,NMR}$[a] (g mol^{-1})	$Đ$[b]	PDGE block		PTEGGE block	
			DP_{PDGE}[c]	ϕ_{PDGE}[d]	DP_{PTEGGE}[e]	ϕ_{PTEGGE}[f]
bicy-BCP-A	21,800	1.06	50	0.49	48	0.51
bicy-BCP-B	22,300	1.03	52	0.50	48	0.50
bicy-BCP-C	22,200	1.03	50	0.51	50	0.49
bicy-BCP-D	22,200	1.04	50	0.49	50	0.51[i]
l-BCP	21,900	1.04	49	0.49	51	0.51

[a]Number-average molecular weight of polymer determined by ^{1}H NMR spectroscopy analysis. [b]Dispersity values determined by size exclusion chromatography (SEC) analysis in THF. [c]Number-average degree of polymerization of PDGE block determined by proton nuclear magnetic resonance (^{1}H NMR) spectroscopy. [d]Volume fraction of PDGE block calculated with the mass densities of cyclic and linear PDGE homopolymers from reference 6. [e]Number-average degree of polymerization of PTEGGE block determined by ^{1}H NMR spectroscopy. [f]Volume fraction of PTEGGE block calculated with the mass densities of cyclic and linear PTEGGE homopolymers from reference 6.

The bicyclic amphiphiles and their linear analogues were subjected to micellization in a variety of organic solvents and solvent mixtures. Consequently, a cosolvent composed of 75 wt% ethanol (EtOH) and 25 wt% deionized water (H_2O) was found to be the optimal condition for stable micellization of the amphiphiles in this study. The micellar solutions for each block copolymer were obtained *via* initial solvation in EtOH followed by the subsequent addition of H_2O. Thereafter, the critical micelle concentration (CMC) for each copolymer micelle was determined *via* X-ray scattering at various copolymer concentrations. When the measured scattering data are converted to invariant Q values and plotted against polymer concentration, as presented in Figure 2, the intersection of two linear extrapolations for each copolymer provides the respective CMC value. Ranging from 0.013 to 0.028 wt%, the determined CMC values show a dependency on the molecular topology; the CMC value is in the order of *bicy*-BCP-C < *bicy*-BCP-D ~ *bicy*-BCP-B < *bicy*-BCP-A < *l*-BCP (Table 2).

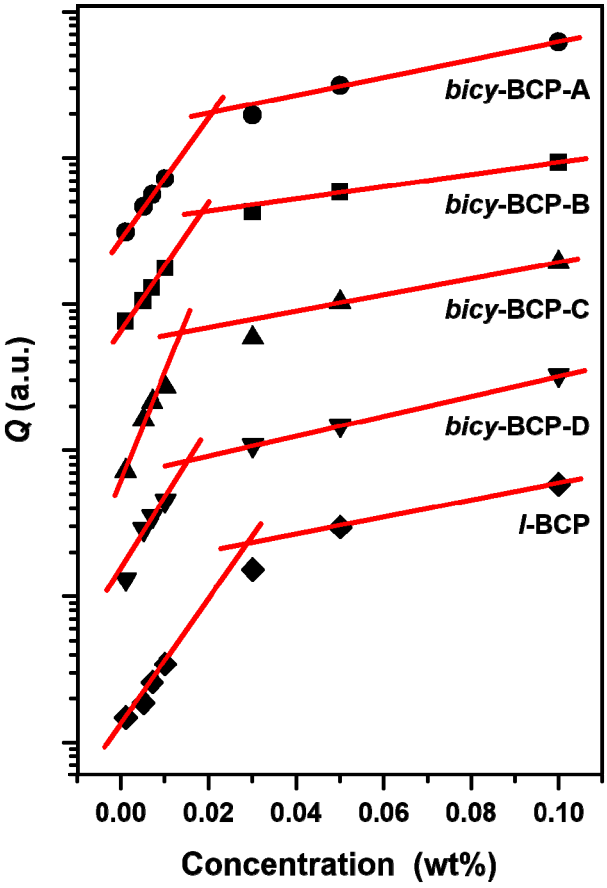

Figure 2. X-ray scattering invariant Q variations of topological amphiphiles as a function of topological copolymer concentration. A mixture of EtOH and H_2O (75/25, wt/wt) was used as the cosolvent.

Table 2. Structural parameters of the micelles of topological block copolymer amphiphiles determined from the invariant, IFT, and Guinier analyses of X-ray scattering data

Topological block copolymer	CMC [a] (wt%)	Structural parameters of micelle						
		D_{max} [b] (nm)	R_{max} [c] (nm)	$R_{g,IFT}$ [d] (nm)	$R_{g,G}$ [e] (nm)	D_{max}/R_{max}	$R_{max}/R_{g,IFT}$	$R_{g,IFT}/R_{g,G}$
bicy-BCP-A	0.021	24.50	10.53	8.01	7.86	2.33	1.31	1.02
bicy-BCP-B	0.018	18.00	7.21	5.52	5.56	2.50	1.31	0.99
bicy-BCP-C	0.013	13.70	6.17	4.68	4.65	2.22	1.32	1.01
bicy-BCP-D	0.017	19.00	6.08	5.08	4.92	3.13	1.20	1.03
l-BCP	0.028	59.00	22.42	18.05	18.57	2.63	1.24	0.97

[a]Critical micelle concentration determined *via* scattering-invariant analysis
[b]Maximum dimension (diameter) of micelles determined using the $p(r)$ function.
[c]Radius of gyration of micelles determined using IFT analysis
[d]Radius of micelles determined from the peak maximum of *the* $p(r)$ profile.
[e]Radius of gyration of micelles determined using Guinier analysis

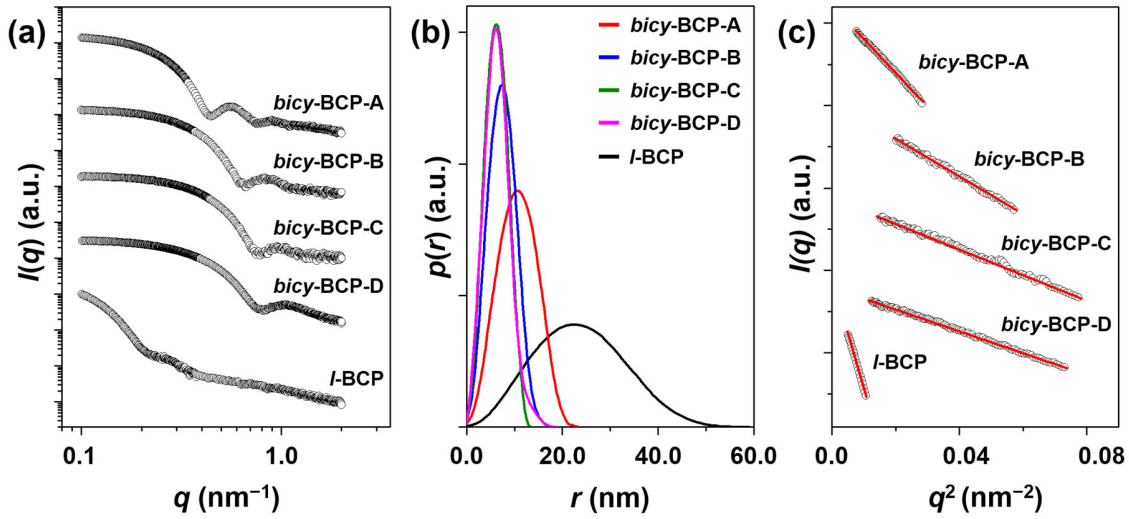

Figure 3. (a) Representative X-ray scattering profiles of topological copolymer micelle solutions with 0.5 wt% concentration in an EtOH/H_2O (75/25, wt/wt) mixture; (b) pair distance distribution functions $p(r)$ obtained from the analysis of the X-ray scattering data in (a); (c) Guinier plots of the X-ray scattering data in (a). Here, $I(q)$ is the scattering intensity at q (magnitude of the scattering vector $\boldsymbol{q}$) and $p(r)$ is the pair distance distribution function that describes the probability of finding two scatterers separated by a distance r inside the micelle. $q = (4\pi/\lambda)\sin\theta$ in which 2θ is the scattering angle and λ is the wavelength of the X-ray beam used.

For each topological amphiphile, the corresponding X-ray scattering profiles of the micelle solutions measured at room temperature are shown in Figure 3a. Each scattering profile was characterized using a combination of the indirect Fourier transformation (IFT) method[8,31-36] and Guinier law[8,32-37] to retrieve various dimensional aspects of micellar structures formed in solution; the details of these analyses are further elaborated in the Supporting Information. IFT analysis, a structure-independent method, offers several dimensional parameters based on the pair distance distribution function $p(r)$ derived from a scattering profile. The determined $p(r)$ profiles and dimensional parameters of topological amphiphiles were found to be strongly dependent on the variations in their bicyclic topologies, as presented in Figure 3b and listed in Table 2. The maximum dimension D_{max} of micelles ranged from 13.70 to 59.00 nm; and D_{max} is found to follow the order of *bicy*-BCP-C < *bicy*-BCP-B < *bicy*-BCP-D << *bicy*-BCP-A << *l*-BCP. Further, the micellar radius R_{max} at the peak maximum of $p(r)$ profile varied from 6.08 to 22.42 nm; and R_{max} was in the following

order: *bicy*-BCP-D < *bicy*-BCP-C < *bicy*-BCP-B << *bicy*-BCP-A << *l*-BCP. Furthermore, the radius of gyration $R_{g,IFT}$ ranged from 4.68−18.05 nm; with $R_{g,IFT}$ in the following order: *bicy*-BCP-C < *bicy*-BCP-D < *bicy*-BCP-B << *bicy*-BCP-A << *l*-BCP.

In addition to establishing relative differences in dimensional parameters between the topological copolymer micelles, certain additional correlations between the aforementioned parameters provide more structural descriptions. As shown in Table 2, the D_{max}/R_{max} ratios range from 2.22 to 3.13, indicating that the micellar shapes are not spherical as the ratio for a perfect sphere is 2. Moreover, the fact that all $R_{max}/R_{g,IFT}$ ratios range from 1.20 to 1.31 is another evidence that the micelle are non-spherical, as $R_{max}/R_{g,IFT}$ for a perfect sphere is 1.36.[38] Based on the difference of $R_{max}/R_{g,IFT}$ values against 1.36, the shape deviation from the sphere is in the following order: *bicy*-BCP-C (1.36 – 1.32 = 0.04) < *bicy*-BCP-A (0.05) ~ *bicy*-BCP-B (0.05) < *l*-BCP (0.12) < *bicy*-BCP-D (0.16). In addition, the topological dependency of $R_{g,IFT}$ is similar to that of $R_{g,G}$ determined by the Guinier law, which considers micelles as an ideal spherical shape (Figure 3c; Table 2). Interestingly, the R_g values obtained by the two methods are in good agreement. However, depending on the topologies, $R_{g,IFT}$ shows a deviation of 1 to 3 % from $R_{g,G}$; and the deviation follows the order: *bicy*-BCP-C ~ *bicy*-BCP-B < *bicy*-BCP-A < *bicy*-BCP-D ~ *l*-BCP. Therefore, these results collectively indicate that all topological copolymer micelles possess non-spherical, globular shapes.

Considering the qualitative analysis results above, the X-ray scattering data were analyzed quantitatively to obtain more detailed structural information on the micelles. All possible structural models were considered, including uniform sphere, core-shell sphere, spherical copolymer micelle, spherical core-fuzzy shell structure, uniform ellipsoid, core-shell ellipsoid, three-phase ellipsoid, and three-phase ellipsoid combined with blobs.[8,39-43] The three-phase ellipsoid model (see Figure S1) combined with blob scattering was used to successfully analyze all scattering data of this study, as shown in Figure 4. The details of this model analysis are presented in the Supporting Information.

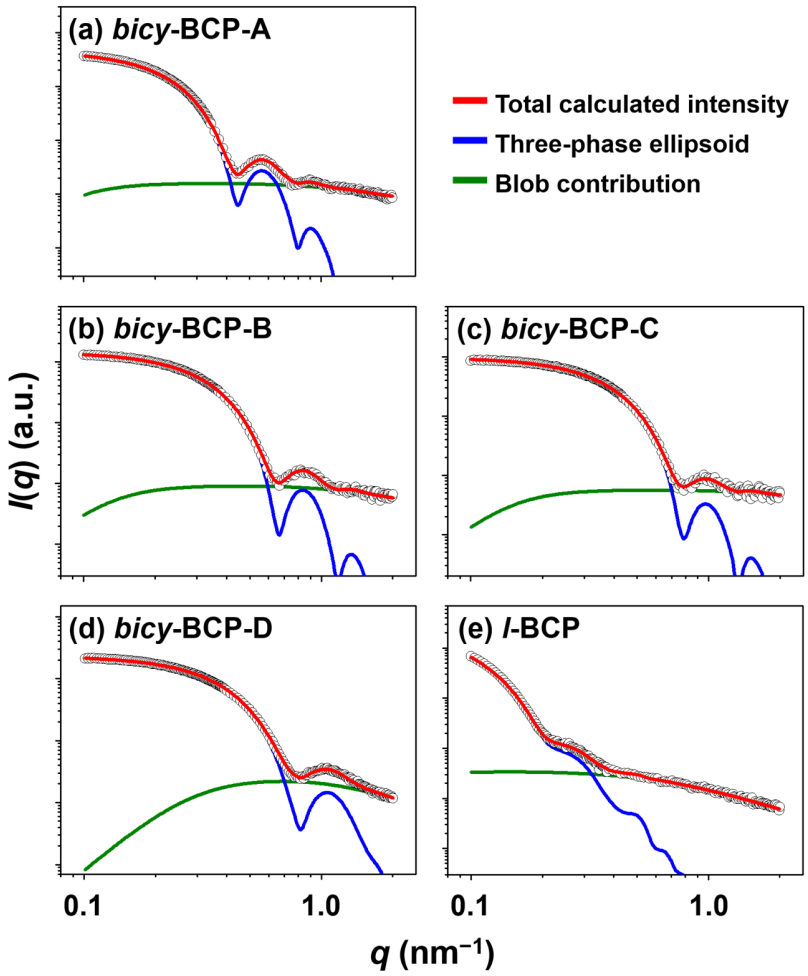

Figure 4. Representative X-ray scattering profiles of topological copolymer micelle solutions: (a) *bicy*-BCP-A; (b) *bicy*-BCP-B; (c) *bicy*-BCP-C; (d) *bicy*-BCP-D; (e) *l*-BCP. The open circles represent the measured scattering intensity, and the red solid lines represent the sum of the calculated intensities obtained *via* data fitting using three-phase ellipsoid model (blue lines) and blob contributions (green lines).

This quantitative analysis confirmed that the individual topological amphiphiles successfully demonstrated the formation of ellipsoidal micelles with unimodal size distributions (Figure 5a). In addition, the micelle size and size distribution exhibited a strong dependency on the molecular topologies. The micelle size ($R_{e,micelle}$, overall radius of micelles in the equatorial direction; R_g, radius of gyration) was in the following order: *bicy*-BCP-D < *bicy*-BCP-C < *bicy*-BCP-B < *bicy*-BCP-A << *l*-BCP (Table 2). However, the determined R_g values and the aforementioned R_g trend are somewhat different from those ($R_{g,IFT}$ and $R_{g,G}$ values in Table 2) estimated using the IFT and Guinier analyses

schemes. The standard deviation $\sigma_{e,micelle}$ (*i.e.*, the apparent broadness of size distribution) for $R_{e,micelle}$ is in the following order: *bicy*-BCP-D < *bicy*-BCP-C < *bicy*-BCP-B < *bicy*-BCP-A << *l*-BCP. However, the $\sigma_{e,micelle}/R_{e,micelle}$ ratio (*i.e.*, more realistic broadness of size distribution) was in the following order: *bicy*-BCP-A ($\sigma_{e,micelle}/R_{e,micelle}$ = 4.6 %) < *bicy*-BCP-B (5.6 %) < *bicy*-BCP-C (6.7 %) < *bicy*-BCP-D (7.8 %) < *l*-BCP (8.1 %).

Thus, the analysis provides further detailed information on the structural shape, ellipsoidicity ε (= $R_{p,micelle}/R_{e,micelle}$ where $R_{p,micelle}$ is the overall polar radius), overall micelle volume $V_{micelle}$, core radius $r_{e,core}$, core volume V_{core} and fraction ϕ_{core}, core density ρ_{core}, dense corona thickness $t_{e,d,corona}$, soft corona thickness $t_{e,s,corona}$, corona volume V_{corona} and fraction ϕ_{corona}, corona density ρ_{corona}, interfacial thicknesses, blob size ξ, average chain aggregation number N_{agg}, and radial density profile (Table 3 and Figure 5b).

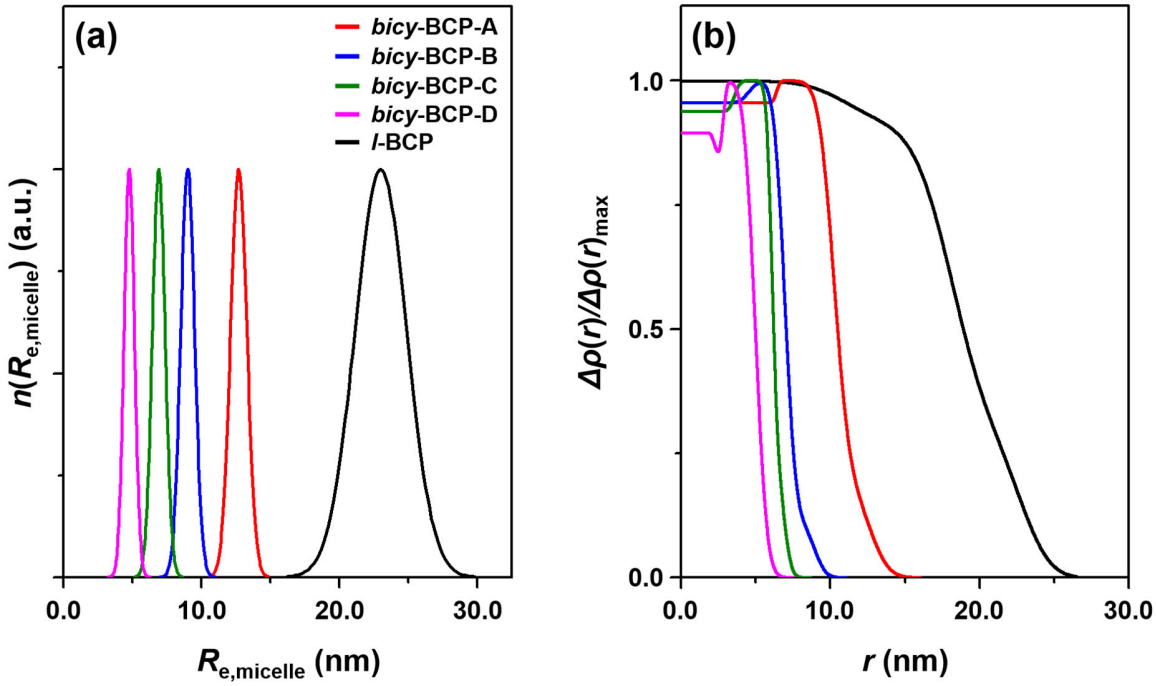

Figure 5. (a) Size distributions and (b) radial density profiles of the micelles assembled by topological bicycles obtained *via* the scattering data analyses in Figure 4. The individual density profiles were normalized to the peak maximum values.

Table 3. Structural parameters of the bicyclic copolymer micelles obtained from the quantitative analysis of scattering data with three-phase ellipsoid model

Structural parameter	Topological copolymer amphiphiles				
	bicy-BCP-A 	*bicy*-BCP –B 	*bicy*-BCP-C 	*bicy*-BCP-D 	*l*-BCP [t] 
$R_{e,micelle}$ [a] (nm)	12.70 (0.59)[b]	9.00 (0.50)	6.90 (0.46)	4.76 (0.37)	23.00 (1.87)
$r_{e,core}$ [c] (nm)	6.40 (0.10)	4.60 (0.10)	3.60 (0.40)	2.48 (0.20)	11.60 (1.00)
$t_{e,f,core}$ [d] (nm)	0.20	0.50	0.30	1.80	2.20
$t_{e,d,corona}$ [e] (nm)	3.90 (0.50)	2.40 (0.45)	2.50 (0.20)	0.95 (0.10)	6.80 (1.50)
$t_{e,f,d.corona}$ [f] (nm)	0.80	0.60	0.30	0.60	2.30
$t_{e,s.corona}$ [g] (nm)	2.40 (0.30)	2.00 (0.20)	0.80 (0.10)	1.33 (0.30)	4.60 (0.50)
$t_{e,f,s.corona}$ [h] (nm)	1.00	0.20	0.50	0.70	2.00
ρ_{core} [i]	0.955	0.956	0.938	0.895	1.000
$\rho_{d.corona}$ [j]	1.000	1.000	1.000	0.750	0.909
$\rho_{s.corona}$ [k]	0.200	0.111	0.250	1.000	0.273
ε [l]	0.81	0.83	0.88	1.30	1.50
ξ [m] (nm)	0.58	0.50	0.30	0.73	1.50
R_g [n] (nm)	9.26	6.60	5.14	4.09	21.20
$V_{micelle}$ [o] (nm^3)	6950.0	2534.5	1210.9	587.3	76447.5
V_{core} [p] (nm^3)	889.4	338.4	172.0	83.1	9807.4
ϕ_{core} [q] (%)	12.8	13.4	14.2	14.1	12.8
ρ_{core} [r] (g cm^{-3})	0.920	0.920	0.920	0.920	1.010
V_{corona} [s] (nm^3)	6060.5	2196.1	1039.9	504.2	66640.1
ϕ_{corona} [t] (%)	87.2	86.6	85.8	85.9	87.2
ρ_{corona} [u] (g cm^{-3})	0.139	0.140	0.144	0.156	0.156
N_{agg} [v]	46	18	9	4	557

[a]Overall radius of the micelle in the equatorial direction. [b]Standard deviation (= $\sigma_{e,micelle}$). [c]Radius of core. [d]Thickness of the fuzzy part (interfaced with the dense corona) of the core [e]Thickness of dense corona. [f]Thickness of the fuzzy part (interfaced with the soft corona) of the dense corona. [g]Thickness of solvated corona. [h]Thickness of the fuzzy part (interfaced with solvent) of the solvated corona. [i]Adjusted electron density of the micelle core. [j]Adjusted electron density of the dense corona. [k]Adjusted electron density of the soft corona. [l]Ellipsoidicity ratio (= [polar radius]/[equatorial radius] = $R_{p,micelle}/R_{e,micelle}$). [m]Average correlation length of density fluctuation (*i.e.*, blob radius) in the corona part. [n]Radius of gyration of micelles [o]Volume of micelles calculated from $R_{p,micelle}$, and $R_{e,micelle}$. [p]Volume of micelle core from $r_{p,core}$ and $r_{e,core}$. [q]Volume fraction of micelle core. [r]Density of core (exclusively considering the PDGE blocks occupied in the core), which is assumed to be equal to that of the PDGE homopolymer in films measured by X-ray reflectivity (XR) analysis in reference 44. [s]Volume of the corona part in the micelle. [t]Volume fraction of the corona. [u]Density of corona part (exclusively accounting for the PTEGGE blocks occupied in the corona), which was estimated from the aggregation number N_{agg} of copolymer chains, number-average molecular weight of the polar block chain, and total volume of the corona part. [v]Average aggregation number of copolymer chains in a single micelle, which was estimated from the core volume and the assumption that the mass density of the core composed of PDGE blocks is equal to that of the PDGE

homopolymer in films measured by XR analysis (see reference 44). [t]Structural parameters of *l*-BCP are from reference 44.

An interesting outcome was the formation of unimodal and oblate ellipsoidal micelles by *bicy*-BCP-A, defined by $R_{p,micelle}$ = 10.29 nm, $R_{e,micelle}$ = 12.70 nm, ε = 0.81, R_g = 9.26 nm, and $V_{micelle}$ = 6950.0 nm^3. In addition, each micelle is assembled by 46 *bicy*-BCP-A molecules (N_{agg}), with the PDGE blocks forming the micelle core with V_{core} = 889.4 nm^3, ϕ_{core} = 12.8 %, ρ_{core} = 0.920 g cm^{-3}, $r_{e,core}$ = 6.40 nm) and a sharp core–relatively dense corona interface ($t_{e,f,core}$ = 0.20 nm). In contrast, the PTEGGE blocks formed the micelle corona composed of a dense and a soft corona layers, wherein the dense corona layer is defined by $t_{e,d.corona}$ = 3.90 nm coupled with a dense–soft corona interface ($t_{e,f,d.corona}$ = 0.80 nm), and the soft corona layer with $t_{e,s.corona}$ = 2.40 nm coupled with a soft corona–solvent interface ($t_{e,f,s.corona}$ = 1.00 nm). Further, the entire micelle corona was estimated to have V_{corona} = 6060.5 nm^3, ϕ_{corona} = 87.2 %, and ρ_{corona} = 0.139 g cm^{-3}. Thus, the micelle corona has a much greater volume and a much lower density than the core. Furthermore, the blob size ξ (*i.e.*, the correlation length for local density fluctuations) was determined to be 0.58 nm. Considering the relatively large density difference between the core and corona, the blob scatterings are expected to have originated from the corona, wherein the dynamic interactions of PTEGGE blocks with the solvent molecules generated density fluctuations. Thus, *bicy*-BCP-A demonstrates the formation of well-defined oblate ellipsoidal micelles with a unimodal narrow size distribution ($\sigma_{e,micelle}$ = 0.59 nm; $\sigma_{e,micelle}/R_{e,micelle}$ = 4.6 %).

The *bicy*-BCP-A micelle described above exhibits a remarkable density profile, as shown in Figure 5b. Moreover, the maximum density instead of occurring at the center of the core (*i.e.*, r = 0 nm), appears at an r value corresponding to the core-dense corona interface, and the center of the micelle core is characterized as approximately 7 % lower than the maximum density value. Further. the density profile beyond the maximum density decreased gradually through the dense and solvated

corona regions, and could be interpreted based on the packing behavior of the cyclic hydrophobic PDGE blocks of *bicy*-BCP-A. Considering the cyclic nature and the absence of a chain end, the cyclic PDGE blocks forming the core would assume a folded chain conformation. When the packing phenomenon is initiated by the side groups, the cyclic hydrophobic blocks transform into a flat, hairpin-like conformation and stack on each other to maximize lateral packing. In this case, the packing density of the side groups is low in the vicinity of the apex of the hairpin conformation owing to increased spacing and strains. Thus, a certain degree of voids (such as molecular voids) may occur in the proximity of the apex of the loop. In contrast, for the side groups positioned along the straighter segments of the hairpin conformation, the packing density is the greatest because there is no increased spacing or strain. However, the packing density abruptly decreases for the side groups located near the conjoining point of the hydrophobic and hydrophilic macrocycles due to multiple factors, such as, the formation of another loop, the greater extent of strains and spacing induced by the conjoining point, and the presence of cyclic hydrophilic blocks in dynamic motion. Thus, this evaluation of the packing ability of cyclic PDGE blocks reveals topological confinement effect that dictates the micellization characteristic for *bicy*-BCP-A. In addition, topological confinement results in the maximum density value not occurring at the center of the micelle core, but at the interface between the core and the dense corona. This feature is clearly distinct from those of the micelles formed by conventional linear diblock copolymers, as well as *l*-BCP.

In addition to the unusual density profile, the overall oblate ellipsoidal micelle of *bicy*-BCP-A is another direct consequence of topological confinement embedded within the bicyclic topology. Given the hairpin-like chain conformation, the PDGE blocks promote a unique aggregation behavior that preferably follows vertical stacking, establishing a flat, two-dimensional plane of copolymer chains that function as the nucleating set for the micelle core formation process. Moreover, the continued vertical stacking of PDGE blocks causes steric hindrance among hydrophilic cyclic PTEGGE chains

owing to their increased hydrodynamic volume from the dynamic chain motion and close proximity. Therefore, to relieve the steric hindrance, the PDGE blocks transition from an ideal vertical packing to a packing form involving curvature causing them to assume intermediate chain conformations that involve a mix of coiled and hairpin-like conformations. This conformational transition reduces the steric hindrance experienced by PTEGGE blocks and decreases the volume, packing density, and length of the PDGE blocks. Consequently, the three-dimensional curvature begins to attain a globular shape, as the micelle formation continues with the addition of more copolymer chains. Furthermore, at the polar axis of the micelle, the chain conformation of hydrophobic cyclic chains possesses the greatest degree of coiled characteristics, thereby producing a polar radius that is shorter than the equatorial radius of the micelle. Thus, the resulting shape of the micelle is an oblate ellipsoid.

Similar characteristics of oblate ellipsoidal micelles were observed with *bicy*-BCP-B. The *bicy*-BCP-B micelle is defined by: $R_{p,micelle}$ = 7.47 nm, $R_{e,micelle}$ = 9.00 nm, ε = 0.83, R_g = 6.60 nm, $V_{micelle}$ = 2534.5 nm^3, $r_{e,core}$ = 4.60 nm with $t_{e,f,core}$ = 0.50 nm, V_{core} = 338.4 nm^3, ϕ_{core} = 13.4 %, ρ_{core} = 0.920 g cm^{-3}, $t_{e,d.corona}$ = 2.40 nm with $t_{e,f,d.corona}$ = 0.60 nm, $t_{e,s.corona}$ = 2.00 nm with $t_{e,f,s.corona}$ = 0.20 nm, V_{corona} = 2196.1 nm^3, ϕ_{corona} = 86.6 %, ρ_{corona} = 0.140 g cm^{-3}, ξ = 0.50 nm, and N_{agg} = 18 (Table 3; Figure 5). Overall, this oblate ellipsoidal micelle exhibits a set of relatively shorter dimensional parameters, a lower degree of ellipsoidal shape distortion, a lower aggregation number, and a narrower size distribution compared to *bicy*-BCP-A micelles.

These distinctive characteristics of *bicy*-BCP-B micelles may originate from the unique block configuration, wherein the PDGE and PTEGGE blocks are arranged in a horizontally oriented hemispherical division, as shown in Figure 1. As each of the two hemicyclic PDGE blocks in *bicy*-BCP-B are half the length of the cyclic PDGE block of *bicy*-BCP-A, hemicyclic PDGE blocks would assume a folded, hairpin-like conformation for optimal lateral packing with a core radius that is roughly half of the *bicy*-BCP-A micelle core. Consequently, the formation of a more compact core

greatly reduces the number of *bicy*-BCP-B chains involved in micellization ($N_{agg,bicy\text{-}BCP\text{-}B} < N_{agg,bicy\text{-}BCP\text{-}A}$). However, despite the lower N_{agg}, the hairpin-like conformation and lateral packing behavior inside the core may be similar to that of *bicy*-BCP-A micelles. In addition, for the corona, two hemicyclic PTEGGE blocks are also half the length of the cyclic PTEGGE block of *bicy*-BCP-A, and they form a thinner corona than that of *bicy*-BCP-A micelles. Thus, the unique molecular topology of *bicy*-BCP-B can lead to the self-assembly of smaller micelles with a lower number of bicyclic molecules.

Similar to the two previous copolymers, *bicy*-BCP-C also formed oblate ellipsoidal micelles. *bicy*-BCP-C micelles exhibit the following structural parameters: $R_{p,micelle}$ = 7.47 nm, $R_{e,micelle}$ = 6.90 nm, ε = 0.88, R_g = 5.14 nm, $V_{micelle}$ = 1210.9 nm^3, $r_{e,core}$ = 3.60 nm ($t_{e,f,core}$ = 0.30 nm), V_{core} = 172.0 nm^3, ϕ_{core} = 14.2 %, ρ_{core} = 0.920 g cm^{-3}, $t_{e,d.corona}$ = 2.50 nm ($t_{e,f,d.corona}$ = 0.30 nm), $t_{e,s.corona}$ = 0.80 nm ($t_{e,f,s,corona}$ = 0.50 nm,), V_{corona} = 1039.9 nm^3, ϕ_{corona} = 85.8 %, ρ_{corona} = 0.144 g cm^{-3}, ξ = 0.30 nm, and N_{agg} = 9 (Table 3; Figure 5). However, in contrast to the micelles of both *bicy*-BCP-A and -B, *bicy*-BCP-C micelles exhibit shorter dimensional parameters, lesser degree of ellipsoidal shape distortion, lower aggregation number, and narrower size distribution. These unique features could be directly correlated with the influence of topological confinement in the block configuration of *bicy*-BCP-C, that is, the PDGE and PTEGGE blocks are arranged in a vertically oriented hemispherical division where the molecular joint conjoining the two macrocycles occurs between the hemicyclic PDGE blocks (Figure 1).

This configuration imposes a strict topological confinement wherein the hemicyclic PDGE blocks are forced to take on multiple chain conformations for optimal packing behavior. The first probable conformation is for the hemicyclic PDGE blocks to assume a flattened, hairpin-like conformation to stack laterally in the most efficient manner. The second option is for the hemicyclic PDGE blocks to assume a hairpin-like conformation, wherein each PDGE block is positioned on two

orthogonal planes rather than a single plane. The third possible conformation would have a pair of hemicyclic PDGE blocks, while individually in a hairpin-like loop conformation, folded over with the molecular joint. However, such a folded conformation may be less favorable from a thermodynamic perspective. Further, considering that $\varepsilon_{bicy\text{-BCP-C}}$ is greater than both $\varepsilon_{bicy\text{-BCP-A}}$ and $\varepsilon_{bicy\text{-BCP-B,}}$ and also closest to unity, it can be deduced that the less distorted ellipsoidal shape results from a reduced degree of lateral stacking inside the core of the *bicy*-BCP-C micelles than the *bicy*-BCP-A and -B micelles. Thus, it is probable that the hemicyclic PDGE blocks of *bicy*-BCP-C assume a complementary combination of the three aforementioned chain conformations to form a less distorted micelle core by favoring three-dimensional packing over lateral packing.

In the case of *bicy*-BCP-D, the influence of topological confinement on the micellar morphology was much more intricate than that of the other bicyclic block copolymers. *bicy*-BCP-D micelles are the most compact of all copolymer micelles in this study, comprised of only four *bicy*-BCP-D molecules (N_{agg}). Moreover, *bicy*-BCP-D micelle is defined by: $R_{p,micelle}$ = 6.19 nm, $R_{e,micelle}$ = 4.76 nm, ε = 1.30, R_g = 4.09 nm, $V_{micelle}$ = 587.3 nm^3, $r_{e,core}$ = 2.48 nm ($t_{e,f.core}$ = 1.80 nm), V_{core} = 83.1 nm^3, ϕ_{core} = 14.1 %, ρ_{core} = 0.920 g cm^{-3}, $t_{e,d.corona}$ = 0.95 nm ($t_{e,f,d.corona}$ = 0.60 nm), $t_{e,s.corona}$ = 1.33 nm ($t_{e,f,s.corona}$ = 0.70 nm,), V_{corona} = 504.2 nm^3, ϕ_{corona} = 85.9 %, ρ_{corona} = 0.156 g cm^{-3}, and ξ = 0.73 nm (Table 3). However, the *bicy*-BCP-D micelle reveals a prolate ellipsoidal shape with ε = 1.30, which is a dramatic difference compared to *bicy*-BCP-A, -B, and -C. Furthermore, the *bicy*-BCP-D micelle has a density profile that is slightly different from those of the other copolymer micelles, wherein the density from the core-dense corona interface undergoes a slight dip before reaching the maximum density in the dense corona region (Figure 5b).

The unique feature of *bicy*-BCP-D is its block configuration, which is the opposite of *bicy*-BCP-C, wherein the vertically oriented hemispherical divisions of PDGE and PTEGGE are the same, but the two macrocycles are connected between the hemicyclic PTEGGE blocks (Figure 1). Considering

the most compact micelle formation, the unique topology of *bicy*-BCP-D places a great strain across the entire block copolymer during micellization because the entire copolymer chain must bend over the molecular joint as the apex for positioning the hemicyclic PDGE blocks into the micelle core. Moreover, the hemicyclic PTEGGE blocks in the bent chain conformation are solvated and actively interacting with the solvent molecules, causing an unfavorable environment for optimal packing of the hemicyclic PDGE blocks; and the position of the molecular joint conjoining the PTEGGE blocks heavily limit the dynamic chain motion range. Therefore, these conformational challenges imposed by the unique topology of *bicy*-BCP-D force the hemicyclic PDGE blocks to adopt a coiled chain conformation rather than the optimal hairpin-like conformation considered in the case of *bicy*-BCP-A, -B, and –C, thereby resulting in a prolate ellipsoid shape rather than an oblate ellipsoid shape. In addition, the bent conformation of the entire copolymer chain caused a significant level of distortion in the prolate ellipsoidal dimensions resulting in the highly strained chain conformation allowing only a low number of bicycle chains to aggregate into micelles.

Prolate ellipsoidal micelle formation was also confirmed for *l*-BCP, which is the linear counterpart of the four bicyclic block copolymers. However, in this case, the micelle exhibits the highest aggregation number of *l*-BCP molecules, highest degree of distortion in its shape, largest size, and widest size distribution. The *l*-BCP micelle defined by the following parameters: $R_{p,micelle}$ = 34.5 nm, $R_{e,micelle}$ = 23.0 nm, ε = 1.50, R_g = 21.20 nm, $V_{micelle}$ = 76447.5 nm^3, $r_{e,core}$ = 11.60 nm ($t_{e,f.core}$ = 2.20 nm), V_{core} = 9807.4 nm^3, ϕ_{core} = 12.8 %, ρ_{core} = 1.010 g cm^{-3}, $t_{e,d.corona}$ = 6.80 nm ($t_{e,f,d.corona}$ = 2.30 nm), $t_{e,s.corona}$ = 4.60 nm ($t_{e,f,s.corona}$ = 2.00 nm,), V_{corona} = 66640.1 nm^3, ϕ_{corona} = 87.2 %, ρ_{corona} = 0.156 g cm^{-3}, ξ = 1.50 nm, and N_{agg} = 557 (Table 3; Figure 5). Moreover, the micelle exhibits a density profile that resembles those commonly observed in micelles assembled using conventional linear diblock copolymer amphiphiles. In addition, the density was found to be the highest at the center of the micelle core, gradually decreasing through the core, followed by a rapid decrease through the

corona. Thus, this density profile is different from that of the *bicy*-BCP-D micelles as well as other bicyclic block copolymer micelles (Figure 5b).

For the *l*-BCP micelle, the $R_{p,micelle}$ value is approximately equal to the length of the *l*-BCP chain in a fully extended conformation (~17 nm), suggesting that the *l*-BCP chains align and pack laterally along the polar axis of the micelle. Given the presence of *n*-decyl side groups in the PDGE blocks, the linear PDGE blocks prefer to orient themselves laterally in a stretched chain conformation to maximize the packing density of the micelle core rather than aggregating in random chain conformations. Thus, it is probable that the chain end of the hydrophobic PDGE block in the linear copolymer is in close proximity to other chain ends from other hydrophobic blocks, resulting in the maximum density occurring at the center of the micelle core. In addition, the equatorial radii are roughly 33 % shorter than the polar radius, suggesting that the copolymer chains along the equatorial plane assume coiled chain conformations. As for the copolymer chains positioned between the polar axis and the equatorial plane of the micelle, a range of intermediate chain conformations between the stretched and coiled chain conformations would be in effect because of the thermodynamic balance between the packing power of the hydrophobic side groups and the interaction of the linear PTEGGE blocks with the solvent molecules. Further, it is probable that the lateral packing among the several linear copolymer chains along the polar axis of the micelle function as the nucleus of the initial growth point for the micelle formation process. However, the continued lateral packing would be disturbed by the active solvent-polymer interactions from the solvation of the hydrophilic blocks, generating a range of dynamic chain motions and a greater hydrodynamic volume of the hydrophilic blocks than hydrophobic blocks. Thus, the steric hindrance experienced by hydrophilic blocks that are in close proximity would be relieved by the hydrophobic blocks gradually adopting the coiled chain character from the stretched conformation with the continuation of the packing phenomenon. In addition, the increase in coiled character results in shortening of the net length of the hydrophobic chain, resulting

in a curvature in the shape of the micelle core nucleus, which allows a greater volume of hydrophilic blocks to spread out. The degree of coiled character reaches the maximum level when the hydrophobic block reaches the equatorial plane of the micelle. Thus, the resulting shape of the micelle is defined by the longer polar axis and shorter equatorial radii, which are prolate ellipsoids.

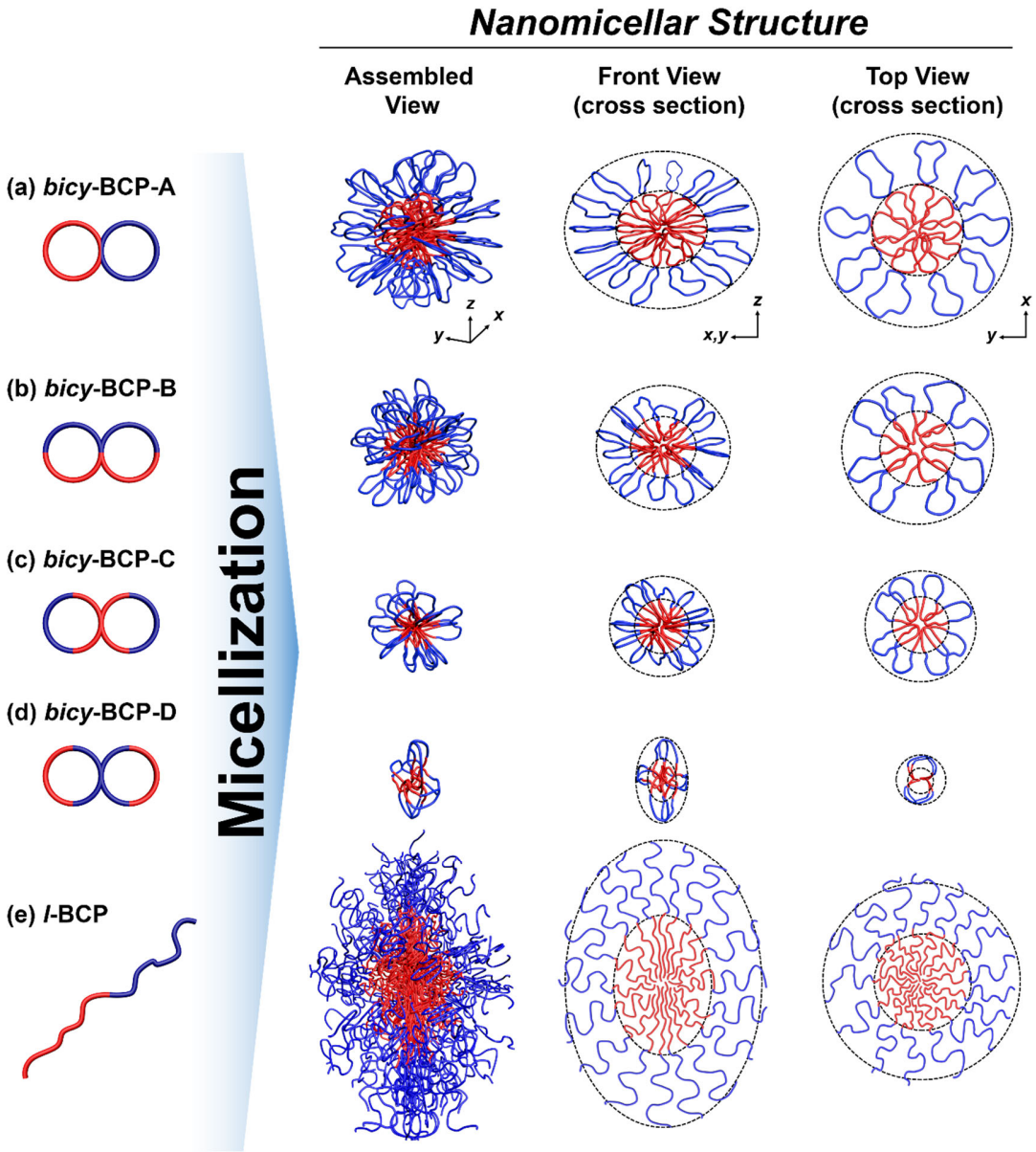

Figure 6. Schematic representations of the nanomicellar structures of topological bicyclic amphiphiles and their linear counterparts, which were sketched with the structural parameters obtained through the quantitative X-ray scattering data analysis using three-phase ellipsoid model.

As discussed above, the quantitative X-ray scattering data analysis confirmed that all four topological bicycle amphiphiles possess drastically different micellization behaviors compared to their linear counterparts and, furthermore, exhibit a diverse set of micellar structural characteristics. Based on the analysis results, including structural parameters and analytical insights, the phase-separated structured micelles of the topological bicycles and their linear counterparts were schematically sketched, as shown in Figure 6.

In addition to the structural shapes and parameters discussed above, it is worth discussing the structural stability of the micelles in terms of topological confinement and dependency. The structural stability of a micelle may be dependent primarily on the stability level of its core and secondarily on the stability of the corona shell. In addition, the micelle stability is reflected by the mode and broadness of the size distribution, and it should be interpreted as a complementary result of the structural integrity of the core and corona. First, the core stability could be understood to be directly proportional to the stability of the entire micelle. Among the structural parameters determined by the quantitative scattering analysis, $t_{e,f,core}$ is the thickness of the fuzzy part (interfaced with the dense corona) of the surface of the core, representing the interfacial sharpness or broadness of the core towards the dense corona with a smaller value indicating a sharper interface between the core and dense corona. Hence, $t_{e,f.core}$ is a direct indicator for evaluating the core stability. The $t_{e,f.core}$ value was found to be in the following order: *bicy*-BCP-A ($t_{e,f.core}$ = 0.20 nm) < *bicy*-BCP-C (0.30 nm) < *bicy*-BCP-B (0.50 nm) << *bicy*-BCP-D (1.80 nm) < *l*-BCP (2.20 nm) (Table 3), which suggests that the core stability is in the following order: *l*-BCP < *bicy*-BCP-D << *bicy*-BCP-B < *bicy*-BCP-C < *bicy*-BCP-A. Second, $t_{e,s.corona}$ and $t_{e,f,s.corona}$ are the thickness of the soft corona (*i.e.*, solvated corona), and the thickness of the interface between the solvated corona and the solvent molecules, respectively,

and they collectively provide information on the degree of volume of the soft corona occupied by the PTEGGE blocks. Smaller $t_{e,s.corona}$, and $t_{e,f,s.corona}$ values represent higher volume occupation of the soft corona, which positively contributes to the stability of the entire corona and can minimize or prevent intermicellar aggregation *via* the impinging process between the soft coronas of multiple micelles. The $t_{e,s.corona}$ value was in the following order: *bicy*-BCP-C < *bicy*-BCP-B < *bicy*-BCP-D < *bicy*-BCP-A << *l*-BCP, while the $t_{e,f,}$ and $_{s.corona}$ values were in the following order: *bicy*-BCP-B < *bicy*-BCP-C < *bicy*-BCP-D < *bicy*-BCP-A < *l*-BCP. These results collectively indicate that the corona stability is in the following order: *l*-BCP << *bicy*-BCP-A < *bicy*-BCP-D < *bicy*-BCP-B ~ *bicy*-BCP-C. Finally, the mode of size distribution was confirmed to be unimodal for all topological copolymers in this study, as discussed earlier. However, the broadness ($\sigma_{e,micelle}/R_{e,micelle}$ ratio) of the size distribution was different from one another. A higher structural integrity of micelles should result in a narrower size distribution. The $\sigma_{e,micelle}/R_{e,micelle}$ ratio was in the following order: *bicy*-BCP-A (0.046) < *bicy*-BCP-B (0.056) < *bicy*-BCP-C (0.067) < *bicy*-BCP-D (0.078) < *l*-BCP (0.081), which suggests the micelle stability is in the following order: *l*-BCP < *bicy*-BCP-D < *bicy*-BCP-C < *bicy*-BCP-B < *bicy*-BCP-A. From these stability evaluations using $t_{e,f.core}$ as a primary indicator and $t_{e,s.corona}$, $t_{e,f,s.corona}$ and $\sigma_{e,micelle}/R_{e,micelle}$ as the secondary factors, it can be concluded that the overall stability of micelles is in the following order: *l*-BCP < *bicy*-BCP-D << *bicy*-BCP-B < *bicy*-BCP-C < *bicy*-BCP-A.

CONCLUSIONS

In this study, the micellization behaviors and resulting micellar structure details of topological bicycles and their linear counterparts, which were composed of hydrophobic PDGE and hydrophilic PTEGGE blocks of equivalent degree of polymerization, were successfully investigated in a co-solvent (75 wt% EtOH and 25 wt% H_2O) using quantitative synchrotron X-ray scattering analysis. The analysis confirmed that they all formed ellipsoidal micelles that revealed unimodal size

distributions. However, the micellization behavior and resultant micellar morphologies are diversified and significantly influenced by topological characteristics (*i.e.*, bicyclic and linear topological types, and block configurations within the bicyclic topology and their embedded topological confinement).

The CMC values were in the following order: *bicy*-BCP-C < *bicy*-BCP-D ~ *bicy*-BCP-B < *bicy*-BCP-A < *l*-BCP. All micelles are ellipsoidal, consisting of a core, dense corona, and soft corona. Further, the degree of ellipsoidal distortion in micellar shape was in the following order: *bicy*-BCP-C < *bicy*-BCP-B < *bicy*-BCP-A < *bicy*-BCP-D < *l*-BCP. *bicy*-BCP-A, -B, and -C exhibit a preference for self-assembly into oblate ellipsoidal micelles, whereas *bicy*-BCP-D and *l*-BCP tend to form prolate ellipsoidal micelles. The chain aggregation numbers of the micelles were in the following order: *bicy*-BCP-D << *bicy*-BCP-C << *bicy*-BCP-B << *bicy*-BCP-A <<< *l*-BCP, while the overall size of the micelles was in the following order: *bicy*-BCP-D < *bicy*-BCP-C < *bicy*-BCP-B < *bicy*-BCP-A << *l*-BCP. The broadness of the size distribution was in the following order: *bicy*-BCP-A < *bicy*-BCP-B < *bicy*-BCP-C < *bicy*-BCP-D < *l*-BCP. The overall volume of micelle followed the order of *bicy*-BCP-D << *bicy*-BCP-C << *bicy*-BCP-B << *bicy*-BCP-A <<< *l*-BCP. The core volume fraction was in the following order: *l*-BCP ~ *bicy*-BCP-A < *bicy*-BCP-B < *bicy*-BCP-D < *bicy*-BCP-C. The *bicy*-BCP-A, -B, and -C micelles possess radial density profiles that are clearly distinct from those of the *bicy*-BCP-D and *l*-BCP micelles. The density profile of the *bicy*-BCP-D micelle was further distinct from that of the *l*-BCP micelles. The overall structural stability of micelles is in the following order: *l*-BCP < *bicy*-BCP-D << *bicy*-BCP-B < *bicy*-BCP-C < *bicy*-BCP-A. These remarkable results collectively indicate that the bicyclic block copolymers form a highly flexible molecular platform for developing a wide variety of nanoscale micelles that may be used for various advanced applications in smart drug delivery, biomedical imaging, cosmetics, food, advanced coating appliances, photonics, and molecular electronics. In particular, the *bicy*-BCP-A-like topology is suitable for producing

highly stable core-shell micelles or particles, while the *bicy*-BCP-C-like topology is suitable for forming small micelles or particles with stable structural integrity.

Associated Content

Supporting Information

The Supporting Information is available free of charge at https://pubs.acs.org/doi

Scattering invariant analysis, indirect Fourier transformation analysis, and three layer ellipsoid model analysis

Author Information

Corresponding Authors

*Email: brianree@eng.hokudai.ac.jp (B.J.R.)

*Email: satoh@eng.hokudai.ac.jp (T.S.)

ORCID

Brian J. Ree: 0000-0002-3959-9896
Kyeong Sik Jin: 0000-0002-0134-9912
Takuya Isono: 0000-0003-3746-2084
Toshifumi Satoh: 0000-0001-5449-9642

Author Contributions

T.S. supervised the project. B.J.R., Y.S., K.S.J. and T.I. designed the experiments, solved the technical issues, and checked the experimental results. All authors contributed to developing the overall scope, interpreting the results and preparing the manuscript.

Notes

The authors declare no competing interests.

Acknowledgements

This study was supported by JSPS Grant-in-Aid for Scientific Research (A and B) (19H00905 and 19H02769 for T.S.), MEXT Grant-in-Aid for Scientific Research on Innovative Areas “Hybrid Catalysis” (20H04789 for T.S.), the Photoexcitonix Project (Hokkaido University, T. S.), Creative Research Institute (CRIS, Hokkaido University, T. S.), and the Frontier Chemistry Center (Hokkaido University, T. S., T. I., and B. J. R.). B. J. R. was funded by the JSPS Fellowship for Young Scientists. The authors thank the Pohang Accelerator Laboratory for providing opportunities to conduct synchrotron X-ray scattering measurements.

References

1. Semlyen, J. A. Cyclic Polymers, 2nd ed., Kluwer Academic Publishers: Dordrecht, Netherlands, 2002.
2. Laurent, B. A.; Grayson, S. M. Synthetic Approaches for the Preparation of Cyclic Polymers. *Chem. Soc. Rev.* **2009**, *38*, 2202–2213.
3. Kricheldorf, H. R. Cyclic Polymers: Synthetic Strategies and Physical Properties. *J. Polym. Sci. Part A: Polym. Chem.* **2010**, *48*, 251−284.
4. Jia, Z.; Monteiro, M.J. Synthesis of Cyclic Polymers via Ring Closure. *Adv. Polym. Sci.* **2013**, *262*, 295−328.
5. Xiang, L.; Ryu, W.; Kim, H.; Ree, M. Precise Synthesis, Properties, and Structures of Cyclic Poly(ε-caprolactone)s. *Polymers* **2018**, *10*, 577.
6. Xiang, L.; Ryu, W.; Kim, J.; Ree, M. Cyclic Topology Effects on the Morphology of Biocompatible and Environment-friendly Poly(ε-caprolactone)s Under Nanoscale Film Confinement. *Polym. Chem.* **2020**, *11*, 4630−4638.
7. Ryu, W.; Xiang, L.; Jeon, T.; Ree, M. Melt Density, Equilibrium Melting Temperature, and Crystallization Characteristics of Highly Pure Cyclic Poly(ε-caprolactone)s. *Polymer* **2020**, *207*, 122899.

8. Ree, B. J.; Satoh, Y.; Jin, K. S.; Isono, T.; Kim, W. J.; Kakuchi, T.; Satoh, T.; Ree, M. Well-Defined Stable Nanomicelles Self-assembled by Brush Cyclic and Tadpole Copolymer Amphiphiles: A Versatile Smart Carrier Platform. *NPG Asia Materials* **2017**, *9*, e453.
9. Zimm, B. H; Stockmayer, W. H. The Dimensions of Chain Molecules Containing Branches and Rings. *J. Chem. Phys*. **1949**, *17*, 1301−1314.
10. Josse, T.; Winter, J. D.; Gerbaux, P.; Coulembier, O. Cyclic Polymers by Ring-Closure Strategies. *Angew. Chem. Int. Ed*. **2016**, *55*, 13944−13958.
11. Li, H.; Debuigne, A.; Jérome, R.; Lecomte, P. Synthesis of Macrocyclic Poly(ε-caprolactone) by Intramolecular Cross-Linking of Unsaturated End Groups of Chains Precyclic by the Initiation. *Angew. Chem. Int. Ed.* **2006**, *45*, 2264−2267.
12. Culkin, D. A.; Jeong, W.; Csihony, S.; Gomez, E. D.; Balsara, N. R.; Hedrick, J. L.; Waymouth, R. M. Zwitterionic Polymerization of Lactide to Cyclic Poly(Lactide) by Using N-Heterocyclic Carbene Organocatalysts. *Angew. Chem. Int. Ed*. **2007**, *46*, 2627−2630.
13. Brown, H. A.; Xiong, S.; Medvedev, G. A.; Chang, Y. A.; Abu-Omar, M. M.; Caruthers, J. M.; Waymouth, R. W. Zwitterionic Ring-Opening Polymerization: Models for Kinetics of Cyclic Poly(caprolactone) Synthesis. *Macromolecules* **2014**, *47*, 2955−2963.
14. Wang, H.; Zhang, L.; Liu, B.; Han, B.; Duan, Z.; Qi, C.; Park, D.; Kim, I. Synthesis of High Molecular Weight Cyclic Poly(ε-caprolactone)s of Variable Ring Size Based on a Light-Induced Ring-Closure Approach. *Macromol. Rapid Commun*. **2015**, *36*, 1646−1650.
15. Ogawa, T.; Nakazono, K.; Aoki, D.; Uchida, S.; Takata, T. Effective Approach to Cyclic Polymer from Linear Polymer: Synthesis and Transformation of Macromolecular [1]Rotaxane. *ACS Macro Lett*. **2015**, *4*, 343−347.
16. Habuchi, S.; Fujiwara, S.; Yamamoto, T.; Tezuka, Y. Single-molecule Imaging Reveals Topological Isomer-dependent Diffusion by 4-armed Star and Dicyclic 8-shaped Polymers. *Polym. Chem.* **2015**, *6*, 4109−4115.
17. Isono, T.; Kamoshida, K.; Satoh, Y.; Takaoka, T.; Sato, S.-i.; Satoh, T.; Kakuchi, T. Synthesis of Star- and Figure-Eight-Shaped Polyethers by *t*-Bu-P$_4$-Catalyzed Ring-Opening Polymerization of Butylene Oxide. *Macromolecules* **2013**, *46*, 3841−3849.
18. Isono, T.; Sasamori, T.; Honda, K.; Mato, Y.; Yamamoto, T.; Tajima, K.; Satoh, T. Multicyclic Polymer Synthesis through Controlled/Living Cyclopolymerization of α,ω-Dinorbornenyl-Functionalized Macromonomers. *Macromolecules* **2018**, *51*, 3855−3864.
19. Mato, Y.; Honda, K.; Tajima, K.; Yamamoto, T.; Isono, T.; Satoh, T. A Versatile Synthetic Strategy for Macromolecular Cages: Intramolecular Consecutive Cyclization of Star-shaped Polymers. *Chem. Sci.* **2019**, *10*, 440−446.
20. Mato, Y.; Honda, K.; Ree, B. J.; Tajima, K.; Yamamoto, T.; Deguchi, T.; Isono, T.; Satoh, T. Programmed Folding into *spiro*-multicyclic Polymer Topologies from Linear and Star-shaped Chains. *Comm. Chem.* **2020**, *3*, 97.
21. Satoh, Y.; Matsuno, H.; Yamamoto, T.; Tajima, K.; Isono, T.; Satoh, T. Synthesis of Well-Defined Three- and Four-Armed Cage-Shaped Polymers *via* "Topological Conversion" from Trefoil- and Quatrefoil-Shaped Polymers. *Macromolecules* **2017**, *50*, 97−106.
22. Fan, X.; Huang, B.; Wang, G.; Huang, J. Synthesis of Amphiphilic Heteroeight-Shaped

Polymer *Cyclic*-[Poly(ethylene oxide)-*b*-polystyrene]$_2$ *via* "Click" Chemistry. *Macromolecules* **2012**, *45*, 3779−3786.
23. Isono, T.; Satoh, Y.; Miyachi, K.; Chen, Y.; Sato, S.-i.; Tajima, K.; Satoh, T.; Kakuchi, T. Synthesis of Linear, Cyclic, Figure-Eight-Shaped, and Tadpole-Shaped Amphiphilic Block Copolyethers via *t*-Bu-P$_4$-Catalyzed Ring-Opening Polymerization of Hydrophilic and Hydrophobic Glycidyl Ethers. *Macromolecules*, **2014**, *47*, 2853−2863.
24. Shingu, T.; Yamamoto, T.; Tajima, K.; Isono, T.; Satoh, T. Synthesis of μ-ABC Tricyclic Miktoarm Star Polymer *via* Intramolecular Click Cyclization. *Polymers* **2018**, *10*, 877.
25. Hatakeyama, F.; Yamamoto, T.; Tezuka, Y. Systematic Synthesis of Block Copolymers Consisting of Topological Amphiphilic Segment Pairs from kyklo- and kentro-Telechelic PEO and Poly(THF). *ACS Macro Letters* **2013**, *2*, 427−431.
26. Shi, G.-Y.; Yang, L.-P.; Pan, C.-Y. Synthesis and Characterization of Well-defined Polystyrene and Poly(ε-caprolactone) Hetero Eight-shaped Copolymers. *J. Polym. Sci. A Polym. Chem.* **2008**, *46*, 6496−6508.
27. Jiang, Y.; Hadjichristidis, N. Polymethylene-based Eight-shaped Cyclic Block Copolymers. *Macromolecules* **2020**, *53*, 267−275.
28. Shi, G.-Y.; Yang, L.-P.; Pan, C.-Y. Well-defined Miktocycle Eight-shaped Copolymers Composed of Polystyrene and Poly(ε-caprolactone): Synthesis and Characterization. *Macromol. Chem. Phys.* **2011**, *212*, 1305−1315.
29. Ree, B. J.; Satoh, Y.; Isono, T.; Satoh, T. Bicyclic Topology Transforms Self-Assembled Nanostructures in Block Copolymer Thin Films. *Nano Lett.* **2020**, *20*, 6520−6525.
30. Ree, B. J.; Satoh, Y.; Isono, T.; Satoh, T. Influence of Topological Confinement on Nanoscale Film Morphologies of Tricyclic Block Copolymers. *Macromolecules* **2021**, *54*, 4120−4127.
31. Glatter, O. Evaluation of Small-angle Scattering Data from Lamellar and Cylindrical Particles by the Indirect Transformaiton Method. *J. Appl. Crystallogr.* **1980**, *13*, 577−584.
32. Shin, S. R.; Jin, K. S.; Lee, C. K.; Kim, S. I.; Spinks, G. M.; So, I.; Jeon, J.-H.; Kang, T. M.; Mun, J. Y.; Han, S.-S.; Ree, M.; Kim, S. J. Fullerene Attachment Enhances Performance of a DNA Nanomachine. *Adv. Mater*. **2009**, *21*, 1907−1910.
33. Jin, S.; Higashihara, T.; Jin, K. S.; Yoon, J.; Heo, K.; Kim, J.; Kim, K.-W.; Hirao, A.; Ree, M. Synchrotron X-ray Scattering Characterization of the Molecular Structures of Star Polystyrenes with Varying Numbers of Arms. *J. Phys. Chem. B* **2010**, *114*, 6247−6257.
34. Jin, K. S.; Shin, S. R.; Ahn, B.; Heo, K.; Kim, S. J.; Ree, M. pH-dependent Structures of an i-motif DNA in Solution. *J. Phys. Chem. B* **2009**, *113*, 1852−1856.
35. Wong, J. C.; Xiang, L.; Ngoi, K. H.; Chia, C. H.; Jin, K. S.; Ree, M. Quantitative Structural Analysis of Polystyrene Nanoparticles Using Synchrotron X-ray Scattering and Dynamic Light Scattering. *Polymers* **2020**, *12*, 477.
36. Jin, K. S.; Rho, Y.; Kim, J.; Kim, H.; Kim, I. J.; Ree, M. Synchrotron X-ray Scattering Studies of the Structure of Porcine Pepsin under Various pH Conditions. *J. Phys. Chem. B* **2008**, *112*, 15821−15827.
37. Guinier, A.; Fournet, G. *Small Angle Scattering X-Ray*, Wiley, New York, 1955.

38. Takeshita, H.; Poovarodom, M.; Kiya, T.; Arai, F.; Takenaka, K.; Miya, M.; Shiomi, T. Crystallization Behavior and Chain Folding Manner of Cyclic, Star and Linear Poly(tetrahydrofuran)s. *Polymer* **2012**, *53*, 5375−5384.
39. Heo, K.; Kim, Y. Y.; Kitazawa, Y.; Kim, M.; Jin, K. S.; Yamamoto, T.; Ree, M. Structural Characteristics of Amphiphilic Cyclic and Linear Block Copolymer Micelles in Aqueous Solutions. *ACS Macro Lett.* **2014**, *3*, 233−239.
40. Pedersen, J. S.; Gerstenberg, M. C. Scattering Form Facto of Block Copolymer Micelles. *Macromolecules* **1996**, *29*, 1363−1365.
41. Pedersen, J. S. Analysis of Small-angle Scattering Data from Colloids and Polymer Solutions: Modeling and Least-squares Fitting. *Adv. Colloid Interface Sci.* **1997**, *70*, 171−210.
42. Ngoi, K. H.; Wong, J. C.; Chiu, W. S.; Chia, C. H.; Jin, K. S.; Kim, H.-J.; Kim, H.-C.; Ree, M. Morphological Structure Details, Size Distributions and Magnetic Properties of Iron Oxide Nanoparticles. *J. Ind. Eng. Chem.* **2021**, *95*, 37−50.
43. Rathgeber, S.; Monkenbusch, M.; Kreitschmann, M.; Urban, V.; Brulet, A. Dynamics of Star-burst Dendrimers in Solution in Relation to Their Structural Properties. *J. Chem. Phys.* **2002**, *117*, 4047.
44. Ree, B. J.; Lee, J.; Satoh, Y.; Kwon, K.; Isono, T.; Satoh, T.; Ree, M. A Comparative Study of Dynamic Light and X-ray Scatterings on Micelles of Topological Polymer Amphiphiles. *Polymers* **2018**, *10*, 1347.
45. Wong, J. C.; Xiang, L.; Ngoi, K. H.; Chia, C. H.; Jin, K. S.; Kim, H.-C.; Kim, H.-J.; Hirao, A.; Ree, M. Molecular Weight Effect on the Structural Detail and Chain Characteristics of 33-armed Star Polystyrene. *Polymer* **2021**, *212*, 123304.

Graphic Table of Contents

Unimodal and Well-Defined Nanomicelles Assembled by Topology-Controlled Bicyclic Block Copolymers

Brian J. Ree,* *Yusuke Satoh*, *Kyeong Sik Jin*, *Takuya Isono*, and *Toshifumi Satoh**